

Distributionally Robust Joint Planning of Coastal Distribution Network and PV–Storage–EV Stations

Wenhao Gao, Yongheng Wang, Wei Chen, Xinwei Shen*

Abstract—The rapid integration of renewable energy resources, such as tidal and photovoltaic (PV) power, coupled with the growing deployment of electric vehicle (EV) charging infrastructure, necessitates coordinated planning for coastal urban distribution networks (DN). This paper presents a tri-layer distributionally robust optimization framework to jointly optimize the siting of PV–storage–EV stations (PSES) and the configuration of coastal DNs, addressing uncertainties related to power load, PV generation, and EV charging demands. At the upper layer, optimal PSES siting and network topology decisions are made to minimize total investment and operational costs. The middle-layer formulation tackles worst-case uncertainty scenarios via the optimal power flow model, utilizing ambiguity sets to capture correlated uncertainties. To handle non-convexities introduced by binary variables for energy storage systems, we propose and rigorously prove the exactness of a novel relaxation approach. At the lower layer, considering the dynamic pricing driven by tidal energy fluctuations, operational decisions—including electricity procurement and carbon emissions are optimized. An inexact column-and-constraint generation (i-C&CG) algorithm is developed for efficient problem-solving. Numerical results from a realistic 47-node coastal DN in China illustrate that the proposed method effectively reduces costs and ensures robust, low-carbon planning under substantial uncertainties.

Index Terms—Coastal distribution network, PV-Storage-EV station, distributionally robust, inexact column-and-constraint generation algorithm.

NOMENCLATURE

Indices and Sets

i, j, k	Index of buses.
ij, jk	Index of branches.
t	Index of time intervals.
u	Index of EVs.
k	Index of areas.
s	Index of scenarios of EV charging.
I	Set of nodes.
L	Set of distribution lines
T	Set of time intervals.
U	Set of EVs.
K	Set of areas.
I_{SUB}, I_k	Set of substation nodes and areas.
S	Set of EV charging scenarios.
$\xi, \xi^P / \xi^Q / \xi^{PV} / \xi^{EV}$	Set of uncertainty, sets of uncertainty parameters of grid / PV / EV.

Parameters

c_{ij}	Construction cost of line ij .
c_i^{PSES}	Construction cost of PSES at node i .
$c_{ij}^{Salt}, c_i^{Salt}$	Additional salt spray cost of Line ij and PSES at node i .
c^{Ele}	Time-of-use (TOU) pricing tariff for electricity.
D_i	Virtual load at node i .
y_k^{min}, y_k^{max}	Minimum and maximum number of PSES in area k .
R_{ij}, X_{ij}	Resistance and reactance of line ij .
S_{ij}^{max}	Maximum complex power of line ij .
V^{min}, V^{max}	Minimum and maximum voltage amplitude of power systems.
$P^{Sub,min}, P^{Sub,max}$	Minimum and maximum active power of substation.
$Q^{Sub,min}, Q^{Sub,max}$	Minimum and maximum reactive power of substation.
$P_{i,t}^{PV,max}$	Maximum active power of PV at node i in time interval t .
$\mu_i^{ESS,ch}, \mu_i^{ESS,dch}$	Charge and discharge efficiency coefficient of ESS at node i .
$P_i^{ESS,min}, P_i^{ESS,max}$	Minimum and maximum active power of ESS at node i .
$E_i^{ESS,min}, E_i^{ESS,max}$	Minimum and maximum capacity of ESS at node i .
π_s^0	Reference probability of EV charging scenario s occurring.
α_1, α_∞	Confidence in the value of the probability distribution of 1-norm and ∞ -norm.
θ_1, θ_∞	Limits of permissible deviations from probability of 1-norm and ∞ -norm.
τ_u	Set of time intervals of EV charging.
$E_{u,0}^{EV}, E_u^{EV}$	Initial and target energy of u -th EV.
$E_u^{EV,min}, E_u^{EV,max}$	Minimum and maximum energy capacity of u -th EV.
$P_u^{EV,max}$	Maximum charging power of u -th EV.
P_0^{Grid}, Q_0^{Grid}	Reference value of active and reactive power of grid.
p_0^{PV}	Reference value of active power of PV.
$\delta p^{P,min}, \delta p^{P,max}$	Minimum and maximum fluctuation range of active power of grid.
$\delta q^{Q,min}, \delta q^{Q,max}$	Minimum and maximum fluctuation range of reactive power of grid.
$\delta p^{PV,min}, \delta p^{PV,max}$	Minimum and maximum fluctuation range of active power of PV.
$P_{t,s}^{EV,ran}$	Random EV charging load cluster in

W. Gao, W. Chen and X. Shen are with Tsinghua Shenzhen International Graduate School, Tsinghua University. Y. Wang is with the Department of Electrical and Electronic Engineering, The University of Hong Kong (Corresponding: X. Shen, sxw.tbsi@sz.tsinghua.edu.cn).

This work is supported in part by National Natural Science Foundation of China (52477102), Guangdong Basic and Applied Basic Research Foundation (2022A1515240019, 2023A1515240055), Excellent Youth Basic Research Fund of Shenzhen (RCYX20231211090430053).

c_k^{CEF}	Carbon tax of area k .
c_t^{TG}, c_t^{TC}	Electricity price from thermal / tidal current units in time interval t .
$P_t^{TG,max}, P_t^{TC,max}$	Maximum power output of thermal / tidal current units in time interval t .
Variables	
y_i/z_{ij}	Binary variable associated with PSES at node i / line ij .
$P_{ij,t}, Q_{ij,t}$	Active and reactive power flow in line ij in time interval t .
$e_{i,t}$	Carbon intensity at node i in time interval t .
$P_{i,t}^{Load}$	Active load at node i in time interval t .
P_t^{TG}/P_t^{TC}	Active power generated by thermal / tidal current units in time interval t .
y_{ij}	Binary variable associated with parent-child node relationship between nodes i and j in radial topology.
F_{ij}	Virtual power flow in line ij .
$P_{i,t}^{Grid}, Q_{i,t}^{Grid}$	Active and reactive power of grid at node i in time interval t .
$P_{i,t}^{EV}$	Charging power of EV at node i in time interval t .
$P_{i,t}^{PV}$	Active power output of PV at node i in time interval t .
$P_{i,t}^{ESS,ch}, P_{i,t}^{ESS,dch}$	Charging and discharging power of ESS at node i in time interval t .
$V_{i,t}$	Voltage magnituder at node i in time interval t .
$P_{i,t}^{Sub}, Q_{i,t}^{Sub}$	Active and reactive power output of substation in time interval t .
$E_{i,t}^{ESS}$	Energy stored of ESS at node i in time interval t .
$\gamma_{i,t}^{ESS,ch}, \gamma_{i,t}^{ESS,dch}$	Binary variable associated with charging and discharging behaviors of ESS at node i in time interval t .
π_s	Probability of EV charging scenario s .
π_s^+/π_s^-	Positive / negative offset of π_s .
$P_{t,s}^{EV,sch}$	Scheduled EV charging load cluster in time interval t for scenario s .
$e_{i,t}^G$	Carbon emission intensity of substation node in time interval t .

I. INTRODUCTION

IN the context of global warming and energy transition, distributed generation resources (DGRs) and EVs have experienced rapid growth and widespread adoption [1]. The evolution of coastal power systems critically depends on the seamless integration of DGRs, EVs, and emerging renewable energy sources such as tidal, floating photovoltaics, and wind power. Incorporating these energy sources into coastal DNS profoundly impacts their power procurement strategies [2].

Previous studies have explored various planning aspects for DNS, EV charging facilities, and DGRs. Some works considered uncertainties in EV charging demand and optimized the placement of DGRs accordingly, yet assumed a fixed DN structure [3]. Reference [4] extended planning to include

network topology jointly with EV charging stations, whereas [5] incorporated traffic flows into EV charging station design but did not integrate multiple types of DGRs. Studies such as [6] and [7] focused on active DNS and intelligent transportation system frameworks involving PV and ESS integration. In [8], PV and ESS are integrated into a unified PSES, and a detailed analysis is conducted on the economic and environmental benefits considering the siting and sizing. Carbon Emission Flow (CEF) is a concept that follows the power flow and has been widely applied to evaluate the rationality of carbon reduction allocation in power systems [9]. Integrating tidal generation can further decrease reliance on thermal power, significantly aiding coastal cities in carbon emission reduction [10]. Additionally, grid-side electricity procurement costs are crucial optimization considerations in DN planning [11]. However, the coordinated planning of low-carbon coastal city DN topology and PSESs siting, considering both grid-side electricity procurement and carbon emission costs, still remains an open research gap.

To model uncertainties in DN and EV station planning, stochastic optimization, robust optimization (RO), and distributionally robust optimization (DRO) methods are frequently employed. The spatio-temporal characteristics of EV charging demand are often modeled using stochastic programming [12], and RO typically focuses on the worst-case scenario to enhance system resilience [13]. DRO combines the advantages of both, which constructs the ambiguity sets of worst-case distributions based on historical spatio-temporal data of EV charging [14]. In the construction of uncertainty sets, Reference [15] imposes a comprehensive norm constraint on the probability distribution of discrete uncertainties. Traditional continuous box-type uncertainty sets for modeling active and reactive loads as well as PV generation, as seen in [16]. However, integrating discrete EV-related uncertainty and continuous load/PV uncertainty in a unified framework has not yet been fully explored.

In terms of algorithms, the column-and-constraint generation (C&CG) algorithm was proposed to efficiently solve two-stage robust optimization problems [17]. To address the challenge of solving master problems in early iterations, the inexact C&CG (i-C&CG) algorithm was developed, which can accelerate convergence by allowing inexact solutions to the master problem while ensuring final solution accuracy through the exploitation and exploration mechanism [18]. The i-C&CG algorithm has been successfully applied in various contexts, such as in [19]. However despite its advantages, applying this algorithm in integrated planning-operation problems for new-type power systems has not yet been fully explored.

To bridge these research gaps, this paper develops a tri-layer distributionally robust planning framework for coastal city DN and PSESs, as illustrated in Fig. 1. The key contributions are summarized as follows:

- 1) A tri-layer coordinated planning model for DN and PSESs in low-carbon coastal cities is developed. The CEF model is introduced to quantify system-wide carbon emissions, facilitating the carbon-aware optimization of power procurement strategies under tidal current generation integration.
- 2) The proposed DRO model accounts for multiple uncer-

tainties, including continuous box-type uncertainty sets for active/reactive loads and PV outputs, as well as discrete ambiguity sets derived from historical data on EV charging demand. To tackle the non-convexity arising from binary variables in the mid-layer, a tailored relaxation strategy for ESS is designed and its exactness is rigorously proved.

3) The i-C&CG algorithm is employed to solve the model efficiently, and its computational superiority over the conventional C&CG method is demonstrated through faster convergence and reduced solution time.

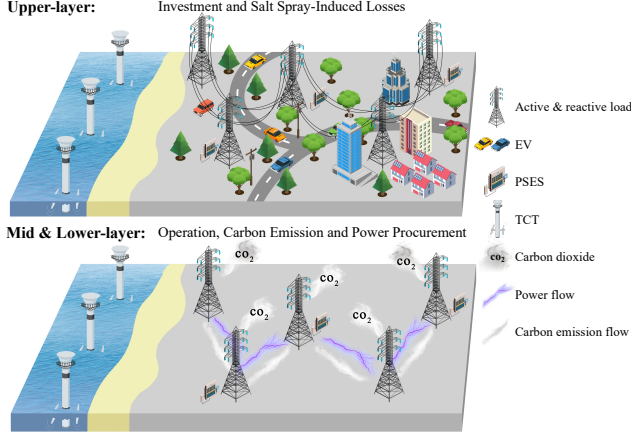


Fig. 1. Schematic diagram of the coupling between the coastal distribution network and PSESs.

The remainder of this paper is structured as follows. Section II introduces the tri-layer coordinated planning model. Section III describes the i-C&CG algorithm developed to solve the resulting convex problem. Section IV presents case studies to validate the effectiveness of the proposed model and algorithm. Finally, conclusions are drawn in Section V.

II. MODEL FORMULATION

A. Objective Function

The objective function incorporates the investment cost of the DN and PSESs, the incremental cost induced by salt spray in the coastal environment, the operational cost arising from DN power losses, the carbon emission cost, and the power procurement cost. The overall objective function is given by:

$$\begin{aligned} \min_{z,y} C^{Inv} + \max_{\substack{\{\pi_s\} \in \xi^{EV} \\ \delta \in \xi^{Grid} \cup \xi^{PV}}} \left\{ \sum_{s \in S} \pi_s \min_{P,Q} C^{Ope} \right\} \\ + \min_{e,P} \left\{ C^{Carb} + C^{Powr} \right\} \end{aligned} \quad (1)$$

1) Investment Cost:

$$\begin{aligned} C^{Inv} = \frac{\rho(1+\rho)^{yr^{Line}}}{(1+\rho)^{yr^{Line}} - 1} \sum_{ij \in L} c_{ij} z_{ij} + \frac{\rho(1+\rho)^{yr^{PSES}}}{(1+\rho)^{yr^{PSES}} - 1} \\ \sum_{i \in I} c_i^{PSES} y_i + \sum_{ij \in L} c_{ij}^{Salt} z_{ij} + \sum_{i \in I} c_i^{Salt} y_i \end{aligned} \quad (2)$$

The objective function (2) minimizes the annualized investment cost associated with the DN in coastal cities and the planning of PSESs, while also accounting for the incremental cost induced by salt spray corrosion in the coastal environment.

In this equation, yr^{Line} and yr^{PSES} represent the expected operational years for distribution network lines and PSESs, the binary decision variables z_{ij} and y_i indicate whether line ij and PSES i are constructed or not, and the parameters c_{ij} and c_i^{PSES} correspond to the associated construction costs. The inflation rate ρ is utilized to convert the total one-time investment costs into equivalent annualized values. Additionally, c_{ij}^{Salt} and c_i^{Salt} represent the annual additional maintenance costs for distribution lines and PSESs caused by salt spray corrosion [20].

2) Operation Cost:

$$C^{Ope} = \eta^{Grid} \sum_{t \in T} \sum_{ij \in L} c^{TOU} R_{ij} (P_{ij,t}^2 + Q_{ij,t}^2) \quad (3)$$

The objective function (3) represents the operational cost of the DN resulting from power losses. In this equation, η^{Grid} denotes the annual number of hours during which the power grid is in operation, which is typically assumed to span the entire year. c^{TOU} reflects the TOU electricity tariff variation between peak and off-peak periods. $P_{ij,t}$ and $Q_{ij,t}$ denote the active and reactive power flows on line ij , respectively, and R_{ij} is the resistance of the corresponding line.

3) Carbon Emission and Power Procurement Cost:

$$C^{Carb} = \eta^{Grid} \sum_{t \in T} \sum_{k \in K} \sum_{i \in I_k} c_k^{CEf} e_{i,t} P_{i,t}^{Load} \quad (4)$$

$$C^{Powr} = \eta^{Grid} \sum_{t \in T} (c_t^{TG} P_t^{TG} + c_t^{TC} P_t^{TC}) \quad (5)$$

The objective function (4) and (5) represent the costs associated with carbon emissions and power procurement for the power grid of the coastal city, respectively. c_k^{CEf} denotes the carbon tax in area k of the city, $e_{i,t}$ is the carbon intensity at node i during each time interval, and $P_{i,t}^{Load}$ represents the active load at the corresponding node. Regarding power procurement costs, P_t^{TG} and P_t^{TC} indicate the active power generated by traditional thermal units and tidal current units, respectively, while c_t^{TG} and c_t^{TC} denote the corresponding electricity prices for each time interval.

B. Constraints

(1) Radial Topology Constraints:

$$\sum_{ij \in L} z_{ij} = |I| \quad (6)$$

$$y_{ij} + y_{ji} = z_{ij} \quad \forall ij \in L \quad (7)$$

$$y_{ij} = 0 \quad \forall i \in I^{SUB}, \forall ij \in L \quad (8)$$

$$\sum_{ij \in L} y_{ij} = 1 \quad \forall i \in I \quad (9)$$

$$\sum_{ij \in L} F_{ij} + D_i = \sum_{ki \in L} F_{ki} \quad \forall i \in I \quad (10)$$

$$|F_{ij}| \leq z_{ij} M \quad \forall ij \in L \quad (11)$$

Cons. (6)–(11) define the radial topology constraints of the DN [21]. Specifically, cons. (6) ensures that the number of lines equals the number of nodes excluding the root node. A binary variable z_{ij} is introduced to indicate whether line ij is connected ($z_{ij} = 1$) or not ($z_{ij} = 0$). Cons. (7)–(9)

impose spanning tree constraints. In particular, cons. (7) guarantees that each connected line maintains a single parent-child relationship: if node $j(i)$ is the parent of node $i(j)$, then y_{ij} (y_{ji}) equals 1. Cons. (8) and (9) enforce that root nodes have no parent node, whereas all other nodes are associated with exactly one parent. Cons. (10)–(11) incorporate single-commodity flow constraints to prevent the formation of pseudo-root nodes. F_{ij} denotes the fictitious flow along line ij , and D_i is the fictitious demand at node i . Cons. (10) ensures flow balance at non-root nodes, while constraint (11) forces F_{ij} to zero when line ij is not connected, utilizing the big-M method.

(2) *Number of PSES Constraint:*

$$y_k^{min} \leq \sum_{i \in I_k} y_i \leq y_k^{max} \quad \forall k \in K \quad (12)$$

In cons. (12), the total number of constructed PSESs is constrained to lie within the bounds of y_k^{min} and y_k^{max} .

(3) *Power Flow Constraints:*

$$\sum_{ij \in L} P_{ij,t} - \sum_{ki \in L} P_{ki,t} = P_{i,t}^{Grid} + y_i P_{i,t,s}^{EV} - y_i P_{i,t}^{PV} + y_i (P_{i,t}^{ESS,ch} - P_{i,t}^{ESS,dch}) \quad \forall i \in I, t \in T, s \in S \quad (13)$$

$$\sum_{ij \in L} Q_{ij,t} - \sum_{ki \in L} Q_{ki,t} = Q_{i,t}^{Grid} \quad \forall i \in I, t \in T \quad (14)$$

$$\begin{aligned} & |V_{i,t}^2 - V_{j,t}^2 - 2(R_{ij}P_{ij,t} + X_{ij}Q_{ij,t})| \\ & \leq (1 - z_{ij})M \quad \forall i, j \in I, ij \in L, t \in T \quad (15) \end{aligned}$$

The Linear DistFlow model is adopted in cons. (13)–(15) to constrain power flow in the radial DN. Cons. (13) ensures active power balance at node i , where the active power flowing out of node i is balanced by the incoming power, considering the contributions from the grid-side load ($P_{i,t}^{Grid}$), PV generation ($P_{i,t}^{PV}$), EV charging demand ($P_{i,t,s}^{EV}$), and the charging/discharging operations of the ESS ($P_{i,t}^{ESS,ch}$, $P_{i,t}^{ESS,dch}$). Similarly, cons. (14) enforces reactive power balance, ensuring that the reactive power flowing into node i is equal to the sum of the reactive load drawn from the grid and the reactive power flowing out. Cons. (15) captures the coupling relationship between voltage magnitude and both active and reactive power flows on distribution lines.

(4) *Grid Security Constraints:*

$$\left\| \begin{array}{c} P_{ij,t} \\ Q_{ij,t} \end{array} \right\|_2 \leq z_{ij} S_{ij}^{max} \quad \forall ij \in L, t \in T \quad (16)$$

$$V^{min} \leq V_{i,t} \leq V^{max} \quad \forall i \in I, t \in T \quad (17)$$

Line capacity and voltage magnitude are limited by cons. (16) and (17) to ensure the security of distribution system.

(5) *Substation Power Constraints:*

$$P^{Sub,min} \leq P_{i,t}^{Sub} \leq P^{Sub,max} \quad \forall i \in I^{SUB}, t \in T \quad (18)$$

$$Q^{Sub,min} \leq Q_{i,t}^{Sub} \leq Q^{Sub,max} \quad \forall i \in I^{SUB}, t \in T \quad (19)$$

The active and reactive power flowing out of the substation are restricted by cons. (18) and cons. (19), respectively.

(6) *PV Operation Constraint:*

$$0 \leq P_{i,t}^{PV} \leq y_i P_{i,t}^{PV,max} \quad \forall i \in I, t \in T \quad (20)$$

The output of PV is constrained by cons. (20) to remain within its maximum generation capacity.

(7) *ESS Operation Constraints:*

$$E_{i,t}^{ESS} = E_{i,t-1}^{ESS} + P_{i,t-1}^{ESS,ch} \mu_i^{ESS,ch} + P_{i,t-1}^{ESS,dch} / \mu_i^{ESS,dch} \quad \forall i \in I, t \in T \quad (21)$$

$$P_i^{ESS,min} \gamma_{i,t}^{ESS,ch} \leq P_{i,t}^{ESS,ch} \leq P_i^{ESS,max} \gamma_{i,t}^{ESS,ch} \quad \forall i \in I, t \in T \quad (22)$$

$$P_i^{ESS,min} \gamma_{i,t}^{ESS,dch} \leq P_{i,t}^{ESS,dch} \leq P_i^{ESS,max} \gamma_{i,t}^{ESS,dch} \quad \forall i \in I, t \in T \quad (23)$$

$$E_i^{ESS,min} \leq E_{i,t}^{ESS} \leq E_i^{ESS,max} \quad \forall i \in I, t \in T \quad (24)$$

$$\gamma_{i,t}^{ESS,ch} + \gamma_{i,t}^{ESS,dch} \leq y_i \quad \forall i \in I, t \in T \quad (25)$$

Cons. (21)–(25) define the operational constraints of the ESS. In cons. (21), the energy stored in the ESS at the beginning of period ($E_{i,t-1}^{ESS}$) is required to equal the energy stored at the end ($E_{i,t}^{ESS}$), accounting for charging and discharging activities, where $\mu_i^{ESS,ch}$ and $\mu_i^{ESS,dch}$ represent the charging and discharging efficiency coefficients, respectively. Cons. (22)–(24) limit the charging power, discharging power, and state of charge of the ESS within their corresponding upper and lower bounds. Finally, cons. (25) ensures that charging and discharging operations of the ESS, denoted by $\gamma_{i,t}^{ESS,ch}$ and $\gamma_{i,t}^{ESS,dch}$, cannot be executed simultaneously.

(8) *Comprehensive Norm Constraints:*

$$\pi_s(\mu) \geq 0 \quad \forall s \in S \quad (26)$$

$$\sum_{s \in S} \pi_s(\mu) = 1 \quad (27)$$

$$\pi_s^{1+}(\mu) + \pi_s^{1-}(\mu) \leq 1 \quad \forall s \in S \quad (28)$$

$$\pi_s^{2+}(\mu) + \pi_s^{2-}(\mu) \leq 1 \quad \forall s \in S \quad (29)$$

$$0 \leq \pi_s^+(\mu) \leq \pi_s^{1+}(\mu) \theta_1 \quad \forall s \in S \quad (30)$$

$$0 \leq \pi_s^-(\mu) \leq \pi_s^{1-}(\mu) \theta_1 \quad \forall s \in S \quad (31)$$

$$0 \leq \pi_s^+(\mu) \leq \pi_s^{2+}(\mu) \theta_\infty \quad \forall s \in S \quad (32)$$

$$0 \leq \pi_s^-(\mu) \leq \pi_s^{2-}(\mu) \theta_\infty \quad \forall s \in S \quad (33)$$

$$\pi_s(\mu) = \pi_s^0(\mu) + \pi_s^+(\mu) - \pi_s^-(\mu) \quad \forall s \in S \quad (34)$$

$$\sum_{s \in S} (\pi_s^+(\mu) + \pi_s^-(\mu)) \leq \theta_1 \quad (35)$$

$$\max_{s \in S} \{\pi_s^+(\mu) + \pi_s^-(\mu)\} \leq \theta_\infty \quad (36)$$

$$\mathbb{P} \left\{ \sum_{s \in S} (\pi_s^+(\mu) + \pi_s^-(\mu)) \leq \theta_1 \right\} \geq 1 - 2|S|e^{-\frac{2|I||T|\theta_1}{|S|}} \quad (37)$$

$$\mathbb{P} \left\{ \max_{s \in S} (\pi_s^+(\mu) + \pi_s^-(\mu)) \leq \theta_\infty \right\} \geq 1 - 2|S|e^{-2|I||T|\theta_\infty} \quad (38)$$

Cons. (26)–(27) constrain the probability of EV charging scenario s occurring, denoted by $\pi_s(\mu)$, where μ represents the mean value of EV charging demand. Cons. (28)–(29) introduce binary auxiliary variables ($\pi_s^{1+}(\mu)$, $\pi_s^{1-}(\mu)$, $\pi_s^{2+}(\mu)$, $\pi_s^{2-}(\mu)$) to linearize the associated constraints. Cons. (30)–(34) define

the relationship between the probability distribution of EV charging and its permissible deviations, where θ_1 and θ_∞ denote the allowable deviation bounds under the 1-norm and ∞ -norm. In these expressions, $\pi_s^0(\mu)$ is the reference probability, while $\pi_s^+(\mu)$ and $\pi_s^-(\mu)$ represent the positive and negative deviations of $\pi_s(\mu)$ from this reference value. Cons. (35) and (36) enforce the norm-based deviation limits under the 1-norm and ∞ -norm. And the confidence levels associated with $\pi_s(\mu)$ are incorporated in cons. (37) and (38) to characterize the reliability of the distributional estimate, where $|S|$, $|I|$, and $|T|$ denote the total number of scenarios, nodes, and time intervals, respectively [22].

The confidence levels for both can be specified as α_1 and α_∞ , respectively. Accordingly, cons. (37) and (38) can be equivalently reformulated as cons. (39) and (40).

$$\mathbb{P} \left\{ \sum_{s \in S} (\pi_s^+(\mu) + \pi_s^-(\mu)) \leq \theta_1 \right\} \geq \alpha_1 \quad (39)$$

$$\mathbb{P} \left\{ \max_{s \in S} (\pi_s^+(\mu) + \pi_s^-(\mu)) \leq \theta_\infty \right\} \geq \alpha_\infty \quad (40)$$

By combining cons. (37)-(40), the expressions for θ_1 and θ_∞ can be derived as follows:

$$\theta_1 = \frac{|S|}{2|I||T|} \ln \frac{2|S|}{1 - \alpha_1} \quad (41)$$

$$\theta_\infty = \frac{1}{2|I||T|} \ln \frac{2|S|}{1 - \alpha_\infty} \quad (42)$$

Cons. (26)–(42) define the comprehensive paradigm constraints, ensuring that the selected probability distribution closely aligns with the actual EV data. Specifically, the initial probability distribution is treated as the center, and a combined norm constraint incorporating both the 1-norm and the ∞ -norm is employed to restrict the deviation of the distribution.

(9) *Carbon Emission Flow Model:*

$$e_{i,t} = \frac{\sum_{ki \in L} P_{ki,t} \rho_{ki,t} + P_{i,t}^G e_{i,t}^G}{\sum_{ki \in L} P_{ki,t} + P_{i,t}^G} \quad \forall i \in I, t \in T \quad (43)$$

$$e_{i,t}^G = \frac{\sum_{t \in T} (P_t^{TG} e_t^{TG} + P_t^{TC} e_t^{TC})}{\sum_{t \in T} (P_t^{TG} + P_t^{TC})} \quad \forall i \in I, t \in T \quad (44)$$

$$\mathbf{P}_I \mathbf{E}_I = \mathbf{P}_L^T \mathbf{E}_I + \mathbf{P}_G^T \mathbf{E}_G \quad (45)$$

$$\mathbf{P}_I = \text{diag} \left[(\zeta_{N+K} (\mathbf{P}_L \oplus \mathbf{P}_G)) \right] \quad (46)$$

$$P_{i,t}^{Load} = P_{i,t}^{Grid} + P_{i,t}^{EV} + P_{i,t}^{ESS,ch} - P_{i,t}^{PV} - P_{i,t}^{ESS,dch} \quad \forall i \in I, t \in T \quad (47)$$

Cons. (43)–(47) characterize the carbon emission flow model in the DN [9]. Expression (43) defines the calculation of carbon intensity, where $\rho_{ki,t}$ denotes the carbon flow density on line ki , $P_{i,t}^G$ is the active power injected into the system by generator sets, and $e_{i,t}^G$ is the carbon emission intensity of the generator located at node i . The value of $e_{i,t}^G$ is

further determined by expression (44), where P_t^{TG} and P_t^{TC} represent the power outputs of thermal and tidal current units, and e_t^{TG} and e_t^{TC} denote their respective carbon emission intensities. By extending cons. (43)–(44) to the system-wide level, cons. (45) is obtained. In this expression, \mathbf{P}_I , \mathbf{P}_L , \mathbf{P}_G , \mathbf{E}_I , and \mathbf{E}_G denote the nodal active power flux matrix, branch power flow distribution matrix, power injection matrix, nodal carbon intensity vector, and generator carbon intensity vector, respectively. Expression (46) specifies the calculation of \mathbf{P}_I , where ζ_{N+K} is a row vector of dimension $N + K$ with all elements equal to 1. The operator “ \oplus ” is defined as the transpose of the concatenation of two matrices. For example, $\mathbf{P}_L \oplus \mathbf{P}_G$ is expressed as: $\begin{bmatrix} \mathbf{P}_L & \mathbf{P}_G \end{bmatrix}^T$. Finally, the active load at node i is calculated by cons. (47).

(10) *Power Procurement Constraints:*

$$P_t^{TG} + P_t^{TC} = \sum_{i \in I} P_{i,t}^{Load} \quad (48)$$

$$0 \leq P_t^{TG} \leq P_t^{TG,max} \quad (49)$$

$$0 \leq P_t^{TC} \leq P_t^{TC,max} \quad (50)$$

Cons. (48) ensures that the total power procured from thermal and tidal current units equals the active load in each time interval. Cons. (49) and (50) impose their respective generation limits.

C. *Uncertainty Scenario Sets*

Uncertainty in this mathematical model arises from load fluctuations and EV charging behaviors. Specifically, the uncertainty in EV charging is discrete, as it is driven by variations in the number of EVs being charged. In contrast, the fluctuations in active and reactive loads of the DN, as well as the power output of PV systems, are continuous in nature.

(1) *EV Charging Behaviors:*

EVs can be incentivized through the TOU electricity tariff to adhere to scheduled charging profiles, thereby facilitating peak load shifting. Under the assumption of full user compliance, the charging behaviors of EVs can be optimized by minimizing the total charging costs:

$$\min \sum_{u \in U} \sum_{t \in \tau_u} c^{Ele} P_{u,t}^{EV} \quad (51)$$

$$s.t. \quad E_u^{EV,min} \leq E_{u,s,0}^{EV(\cdot)} + \sum_{t \in \tau_u} P_{u,t,s}^{EV} \leq E_u^{EV,max} \quad \forall u \in U, t \in \tau_u, s \in S \quad (52)$$

$$E_{u,s,0}^{EV(\cdot)} + \sum_{t \in \tau_u} P_{u,t,s}^{EV} \geq E_{u,s}^{EV(\cdot)} \quad \forall u \in U, s \in S \quad (53)$$

$$\sum_{t \in T - \tau_u} \sum_{u \in U} P_{u,t,s}^{EV} = 0 \quad \forall s \in S \quad (54)$$

$$0 \leq P_{u,t,s}^{EV} \leq P_u^{EV,max} \quad \forall u \in U, t \in \tau_u, s \in S \quad (55)$$

$$P_{i,s}^{EV,sch} = \sum_{u \in U} P_{u,t,s}^{EV} \quad \forall t \in \tau_u, s \in S \quad (56)$$

$$P_{i,s}^{EV} = \max \left\{ P_{i,s}^{EV,ran}, P_{i,s}^{EV,sch} \right\} \quad \forall t \in \tau_u, s \in S \quad (57)$$

where $P_{u,t,s}^{EV}$, $E_{u,s,0}^{EV(\cdot)}$ and $E_{u,s}^{EV(\cdot)}$ are the charging power of u -th EV, the initial battery state of charge (SoC) considering the uncertain behaviors (\cdot) and the corresponding target SoC.

Cons. (52) limits the relationship between the capacity and charging power of EVs. Cons. (53) ensures that the target SoC is satisfied. Cons. (54) enforces that EVs stop charging upon departure from the PSEs, and the bounds of EV charging power are defined in cons. (55). In expression (56), the aggregate charging power of all EVs under the scheduled strategy ($P_s^{EV,sch}$), is determined for each time interval t and scenario s . Meanwhile, considering the possibility that EVs may not fully follow the scheduled strategy, a set of random charging scenarios is introduced in cons. (57). For each time interval and scenario, the uncertainty set is constructed by taking the maximum value between the scheduled and random charging power profiles.

(2) Uncertainty Scenario Set:

The uncertainties of PV power output and grid load are represented using box-type uncertainty sets, as defined in (58)–(60), respectively. In contrast, due to the discrete nature of the number of EVs requiring charging, the EV charging power in (61) is assumed to follow a truncated normal distribution, with the mean determined by the expectation based on the scenario probability π_s , variance σ^2 , and bounded by the EV population limits μ_s^{\min} and μ_s^{\max} .

$$\xi^P = \left\{ P_{i,t}^{Grid} \mid P_0^{Grid} - \delta p^{P,min} \leq P_{i,t}^{Grid} \leq P_0^{Grid} + \delta p^{P,max} \right\} \quad \forall i \in I, t \in T \quad (58)$$

$$\xi^Q = \left\{ Q_{i,t}^{Grid} \mid Q_0^{Grid} - \delta q^{Q,min} \leq Q_{i,t}^{Grid} \leq Q_0^{Grid} + \delta q^{Q,max} \right\} \quad \forall i \in I, t \in T \quad (59)$$

$$\xi^{PV} = \left\{ P_{i,t}^{PV} \mid P_0^{PV} - \delta p^{PV,min} \leq P_{i,t}^{PV} \leq P_0^{PV} + \delta p^{PV,max} \right\} \quad \forall i \in I, t \in T \quad (60)$$

$$\xi^{EV} = \left\{ P_{i,t}^{EV} \mid P_{i,t}^{EV} \sim \Psi \left(\sum_{s \in S} \pi_s \mu_s, \sigma^2, \mu_s^{\min}, \mu_s^{\max} \right) \right\} \quad \forall i \in I, t \in T \quad (61)$$

Therefore, the joint consideration of continuous and discrete uncertainty sets can be expressed in the unified form (62).

$$\xi = \{ \xi^P, \xi^Q, \xi^{PV}, \xi^{EV} \} \quad (62)$$

III. SOLUTION METHOD WITH I-C&CG ALGORITHM

A. Compact Formulation of the Optimization Model

The mathematical problem can be structured as a tri-layer model: the upper-layer determines the planning of the DN and PSEs; the mid-layer optimizes their operation; and the lower-layer determines the power procurement strategy in response to the coastal city's low-carbon policies and urban characteristics. For clarity, the compact form of the proposed model is summarized below and detailed in (63)–(67).

$$\min_{\mathbf{z}, \mathbf{y}} f(\mathbf{z}, \mathbf{y}) + \max_{\delta} \min_{\mathbf{p}, \mathbf{q}} g(\mathbf{p}^2, \mathbf{q}^2) + \min_{\mathbf{p}, \mathbf{e}} h(\mathbf{p}, \mathbf{e}) \quad (63)$$

$$s.t. \quad \mathbf{A}\mathbf{z} + \mathbf{B}\mathbf{y} \geq \mathbf{b} \quad (64)$$

$$\mathbf{C}\mathbf{z} + \mathbf{D}\mathbf{y} + \mathbf{d} \geq \mathbf{E}\mathbf{p} + \mathbf{F}\mathbf{q} + \mathbf{G}\delta \quad (65)$$

$$\mathbf{H}\mathbf{z} + \mathbf{I}\mathbf{y} + \mathbf{k} \geq \mathbf{J}\mathbf{p} + \mathbf{K}\mathbf{q} + \mathbf{L}\mathbf{e} + \mathbf{M}\delta \quad (66)$$

$$\mathbf{z} \in \mathbb{S}_{\mathbf{z}}, \mathbf{y} \in \mathbb{S}_{\mathbf{y}}, \mathbf{p} \in \mathbb{S}_{\mathbf{p}}, \mathbf{q} \in \mathbb{S}_{\mathbf{q}}, \mathbf{e} \in \mathbb{S}_{\mathbf{e}}, \delta \in \xi \quad (67)$$

where \mathbf{z} and \mathbf{y} represent the decision variables associated with distribution lines and PSEs, \mathbf{p} and \mathbf{q} denote the active and reactive power variables, \mathbf{e} indicates the system-wide carbon intensity, and δ refers to the uncertainty scenarios. The upper-layer objective $f(\mathbf{z}, \mathbf{y})$ in (63) captures the investment cost, formulated in equation (2) and constrained by (64)–(65), which correspond to cons. (6)–(12) and (13)–(42). The mid-layer operation objective $g(\mathbf{p}^2, \mathbf{q}^2)$ aligns with equation (3), sharing constraints in (65). At the lower layer, $h(\mathbf{p}, \mathbf{e})$ is defined by equations (4)–(5), addressing carbon emissions and power procurement costs, subject to (66) corresponding to cons. (43)–(50). A–M denote coefficient matrices, while \mathbf{b} , \mathbf{d} , and \mathbf{k} are the corresponding vectors in the constraints. Additionally, $\mathbb{S}_{(\cdot)}$ defines the feasible regions for each decision variable, and ξ represents the holistic uncertainty set.

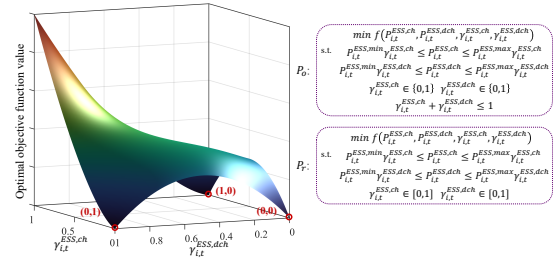


Fig. 2. A small example for feasibility analysis.

Due to the presence of binary decision variables in the ESS-related constraints in the mid-layer, the problem is strongly non-convex and computationally intensive. Consequently, it cannot be addressed using Karush-Kuhn-Tucker (KKT) conditions or other convex optimization techniques. To resolve this challenge, we relax the binary variables ($\gamma_{i,t}^{ESS,ch}$, $\gamma_{i,t}^{ESS,dch}$) and demonstrate that the relaxation is exact. As shown in Fig. 2, the original ESS optimization problem can be expressed as \mathbf{P}_o , and its relaxed version is referred to as \mathbf{P}_r , which expands the feasible region from \mathcal{F}_o to \mathcal{F}_r . Let $(\gamma_{i,t}^{ESS,ch*}, \gamma_{i,t}^{ESS,dch*})$ be the optimal solution to \mathbf{P}_r , with the corresponding optimal objective value given by $f^* = \min_{(\gamma_{i,t}^{ESS,ch}, \gamma_{i,t}^{ESS,dch}) \in \mathcal{F}_r} f(\gamma_{i,t}^{ESS,ch}, \gamma_{i,t}^{ESS,dch})$. Because the charging efficiency $\mu_i^{ESS,ch}$ is less than 1 and the discharging efficiency $\mu_i^{ESS,dch}$ is greater than 1, simultaneous charging and discharging within the same time interval leads to additional energy losses, thereby increasing the objective value. Thus, even if $\gamma_{i,t}^{ESS,ch}$ and $\gamma_{i,t}^{ESS,dch}$ are relaxed to $[0, 1]$, any optimal solution forces at least one of these variables to be zero. Moreover, the feasible region in (22) and (23) remain unchanged under this relaxation. As a result, any solution in \mathbf{P}_r can be mapped to a binary solution $(\gamma_{i,t}^{ESS,ch*}, \gamma_{i,t}^{ESS,dch*}) \in \{0, 1\}$, which belongs to \mathcal{F}_o . Hence,

$$\min_{(\gamma_{i,t}^{ESS,ch}, \gamma_{i,t}^{ESS,dch}) \in \mathcal{F}_o} f(\gamma_{i,t}^{ESS,ch}, \gamma_{i,t}^{ESS,dch}) \leq f(\gamma_{i,t}^{ESS,ch*}, \gamma_{i,t}^{ESS,dch*}) = f^*.$$

Since $\mathcal{F}_o \subset \mathcal{F}_r$, it also follows that

$$\min_{(\gamma_{i,t}^{ESS,ch}, \gamma_{i,t}^{ESS,dch}) \in \mathcal{F}_o} f(\gamma_{i,t}^{ESS,ch}, \gamma_{i,t}^{ESS,dch}) \geq \min_{(\gamma_{i,t}^{ESS,ch}, \gamma_{i,t}^{ESS,dch}) \in \mathcal{F}_r} f(\gamma_{i,t}^{ESS,ch}, \gamma_{i,t}^{ESS,dch}) = f^*.$$

Combining these two inequalities above gives

$$\begin{aligned} & \min_{(\gamma_{i,t}^{ESS,ch}, \gamma_{i,t}^{ESS,dch}) \in \mathcal{F}_o} f(\gamma_{i,t}^{ESS,ch}, \gamma_{i,t}^{ESS,dch}) \\ &= \min_{(\gamma_{i,t}^{ESS,ch}, \gamma_{i,t}^{ESS,dch}) \in \mathcal{F}_r} f(\gamma_{i,t}^{ESS,ch}, \gamma_{i,t}^{ESS,dch}) = f^*. \end{aligned}$$

Therefore, as illustrated in Fig. 2, the ESS retains its three operating modes (charging, discharging, or idle), verifying that the relaxation is exact. Leveraging the exactness, the KKT conditions are applied to reformulate the original bi-level “max min” problem into a single-level “max” problem, as shown in (68)–(74).

$$\max_{\delta, \mathbf{p}, \mathbf{q}} g(\mathbf{p}^2, \mathbf{q}^2) \quad (68)$$

$$s.t. \quad (\mathbf{Cz} + \mathbf{Dy} - \mathbf{Ep} - \mathbf{Fq} - \mathbf{G}\delta + \mathbf{d})_i \geq 0 \quad \forall i \quad (69)$$

$$(\mathbf{Cz} + \mathbf{Dy} - \mathbf{Ep} - \mathbf{Fq} - \mathbf{G}\delta + \mathbf{d})_i \leq M(1 - \omega_i) \quad \forall i \quad (70)$$

$$0 \leq \lambda_i \leq M\omega_i \quad \forall i \quad (71)$$

$$\nabla_{\mathbf{p}} g(\mathbf{p}^2, \mathbf{q}^2) + (\mathbf{E}^T \lambda)_i = 0 \quad \forall i \quad (72)$$

$$\nabla_{\mathbf{q}} g(\mathbf{p}^2, \mathbf{q}^2) + (\mathbf{F}^T \lambda)_i = 0 \quad \forall i \quad (73)$$

$$\mathbf{p} \in \mathbb{S}_{\mathbf{p}}, \mathbf{q} \in \mathbb{S}_{\mathbf{q}}, \delta \in \xi, \lambda \in \mathbb{R}_+, \omega \in \{0, 1\} \quad (74)$$

where i indicates the index of constraints (65), and λ_i is the Lagrange multiplier. Cons. (69) is the constraints of primal problem, cons. (70)–(73) are linearized complementary slackness conditions by *big-M* method and the constraints of dual problem. In (74), \mathbb{R}_+ denotes the set of positive real numbers, and ω is the introduced auxiliary binary variables for complementary slackness.

The CEF is a virtual flow that evolves along with the physical power flow, capturing the distribution characteristics of carbon emissions throughout the processes of generation, transmission, and consumption. As CEF is derived based on the results of system planning and operation, it generally does not affect the planning of the distribution network or the siting of PSESs [9], [23]. Similarly, the power procurement strategy of the coastal city does not influence the upper two layers. Therefore, the third-layer problem (the layer of carbon emissions and power procurement) can be decoupled from the upper two layers. Consequently, the optimal solutions $\mathbf{z}^*, \mathbf{y}^*, \mathbf{p}^*, \mathbf{q}^*$ obtained from the upper two layers can be substituted into the third-layer problem. The compact form of the layer after decoupling is presented in (75)–(77).

$$\min_{\mathbf{p}', \mathbf{e}} h(\mathbf{p}', \mathbf{e}) \quad (75)$$

$$s.t. \quad \mathbf{H}\mathbf{z}^* + \mathbf{I}\mathbf{y}^* + \mathbf{k} \geq \mathbf{J}(\mathbf{p}^* + \mathbf{p}') + \mathbf{K}\mathbf{q}^* + \mathbf{L}\mathbf{e} + \mathbf{M}\delta^* \quad (76)$$

$$\mathbf{p}' \in \mathbb{S}_{\mathbf{p}}, \mathbf{e} \in \mathbb{S}_{\mathbf{e}} \quad (77)$$

where \mathbf{p}' denotes the active power in the third layer.

B. Inexact Column-and-Constraint Generation Algorithm

After decoupling the third layer, the upper two layers are reformulated as a two-stage DRO problem, where the upper layer passes the DN topology \mathbf{z}^* and PSESs siting decisions \mathbf{y}^* to the mid-layer. In return, the mid-layer provides the scenario δ^* and the corresponding scenario-dependent constraints (69)–(73) back to the upper layer. This reformulated problem can be effectively solved using the i-C&CG algorithm. The algorithm is initialized in Step 1 by setting the necessary parameters. In each iteration, the master problem is solved with a relative optimality gap ε_i^{MP} , yielding the upper bound

UB_i and the lower bound LB_i . If the solution is valid ($LB_i \geq \overline{LB}$), the index ℓ is updated to the current iteration to indicate the most recently valid solution. \overline{LB} is then updated to UB_i to accelerate the improvement of the lower bound in the next iteration of the master problem. With the optimal solution from the master problem fixed, the subproblem is solved to identify the worst-case scenario δ_i^* and its corresponding optimal value, following the traditional C&CG procedure. If \overline{UB} and UB_i are sufficiently close, the algorithm enters the exploitation phase with a backtracking routine (Step 11), which leverages the most recent valid lower bound LB_ℓ and returns to Step 3 to re-solve the master problem based on LB_ℓ using the reduced relative gap $\alpha\varepsilon_i^{MP}$ to correct the inaccuracies in the previous iteration. Otherwise, the algorithm proceeds to the exploration phase by enlarging the scenario set as in the C&CG algorithm. The algorithm terminates when the convergence criterion $(\overline{UB} - LB_\ell)/\overline{UB} < \varepsilon$ is satisfied.

Algorithm 1: i-C&CG Algorithm for Solving Two-Stage DRO Problem

- 1: **Initialize:** $\overline{LB} = 0, \overline{UB} = +\infty, i = 1, \ell = 0, \xi = \emptyset, \varepsilon \in [0, 1], \tilde{\varepsilon} \in (0, \varepsilon/(\varepsilon + 1)), \varepsilon_i^{MP}, \alpha \in (0, 1)$.
 - 2: **while** $(\overline{UB} - LB_\ell)/\overline{UB} \geq \varepsilon$ **do**
 - 3: Within a relative optimality gap ε_i^{MP} , solve the **Master Problem**:

$$v_i^* = \min_{\mathbf{z}, \mathbf{y}} f(\mathbf{z}, \mathbf{y}) + \eta$$

$$s.t. \quad \eta \geq g(\mathbf{p}, \mathbf{q}),$$

$$f(\mathbf{z}, \mathbf{y}) + \eta \geq \overline{LB},$$
 Cons. (64), (69)–(73).
 - 4: Record the optimal solution $(\mathbf{z}_i^*, \mathbf{y}_i^*, \eta_i^*)$.
 - 5: Record a valid lower bound $LB_i \geq \overline{LB}$ and an upper bound $UB_i = v_i^*$. If $LB_i \geq \overline{LB}$, then set $\ell \leftarrow i$.
 - 6: Update $\overline{LB} = UB_i$.
 - 7: For fixed $\mathbf{z} = \mathbf{z}_i^*$ and $\mathbf{y} = \mathbf{y}_i^*$, solve the **Subproblem**:

$$D_i^* = \max_{\delta, \mathbf{p}, \mathbf{q}} g(\mathbf{p}, \mathbf{q})$$

$$s.t. \quad \text{Cons. (69)–(73)}.$$
 - 8: Record the worst scenario δ_i^* and its optimal value D_i^* .
 - 9: Update $\overline{UB} = \min\{\overline{UB}, f(\mathbf{z}_i^*, \mathbf{y}_i^*) + D_i^*\}$.
 - 10: **if** $(\overline{UB} - UB_i)/\overline{UB} < \tilde{\varepsilon}$ **then**
 - 11: **Exploitation:** Set $i \leftarrow \ell, \overline{LB} = LB_\ell$, update $\varepsilon_i^{MP} = \alpha\varepsilon_i^{MP}$ for all $i \geq \ell$ with **Backtracking Routine**.
 - 12: **break**
 - 13: **else**
 - 14: **Exploration:** Enlarge the scenario set $\xi = \xi \cup \{\delta_i^*\}$, update
 - 15: $i \leftarrow i + 1$.
 - 16: **end if**
 - 17: **end while**
 - 18: **Output:** Return the optimal solution $(\mathbf{z}_{i-1}^*, \mathbf{y}_{i-1}^*)$ for which $obj^* = \overline{UB}$.
-

IV. CASE STUDIES

The proposed model is tested on a 47-node DN located in Longgang District, Shenzhen, China [6]. The construction cost of distribution lines is 23.30×10^4 CNY/km. The investment cost for the conventional EV charging station is 187×10^4 CNY/unit, while that for the PSES is 344.5×10^4 CNY/unit, comprising PV systems with the peak power of 75kW and an ESS with 1.5 MWh storage, 0.2 MW charging, and 0.3 MW discharging power. PV installations receive a 1 CNY/W upfront subsidy and 0.05 CNY/kWh energy subsidy, while ESSs receive 0.9 CNY/Wh installation and 12 CNY/kWh capacity standby subsidies. The salt spray degradation coefficients are 0.03 for distribution lines and 0.02 for charging stations. All components follow a discount rate of 0.05, with design lives of 20 years for distribution lines and EV

stations, 30 years for PV, and 25 years for ESS. The voltage magnitude is constrained within the range of 0.9 to 1.1 p.u. to ensure acceptable operating conditions. The thermal unit has a 30 MW capacity, 0.85 t/MWh carbon intensity, and a 0.4 CNY/kWh procurement cost. Installed tidal capacity is 9 MW; other parameters are detailed in Fig. 7(a). Shenzhen's TOU tariffs are 1.11 CNY/kWh (peak), 0.65 CNY/kWh (off-peak), and 0.25 CNY/kWh (standard) [7]. Carbon prices are 50 CNY/t for industrial zones, 40 CNY/t for commercial/office areas, and 30 CNY/t for residential areas. Both α_1 and α_∞ for the EV-related mean distribution are set to 0.99, the variance of the truncated normal distribution to 0.12, and the confidence level to 0.95.

A. Simulation Results

To evaluate the effectiveness of PSEs against conventional EV charging stations, the benefits of coordinated planning between coastal distribution networks and PSEs, and the computational efficiency of the i-C&CG algorithm, four distinct cases are presented. The model was formulated using the YALMIP tool in MATLAB (2021a) and evaluated with the GUROBI Optimizer (9.5.2) on the Apple M3 Pro (12-core CPU, 18-core GPU). The four cases are outlined as follows:

Case A: Coordinated planning of costal DN and conventional EV charging stations with C&CG algorithm

Case B: Coordinated planning of costal DN and conventional EV charging stations with i-C&CG algorithm

Case C: Coordinated planning of costal DN and PSEs with i-C&CG algorithm

Case D: Planning of costal DN without considering the siting of PSEs with i-C&CG algorithm

The convergence gap for the algorithms in this study is set to 1%, and at least one PSES is required to be deployed in each area. The planning results of distribution lines and PSEs, along with the corresponding costs and solution time for the four cases are presented in Fig. 8 and Table I.

TABLE I
ANNUALIZED COSTS(10^4 CNY ¥) AND SOLUTION TIME(S)

Case No.	Case A	Case B	Case C*	Case D
DN	✓	✓	✓	✓
PSES	—	—	✓	✓
i-C&CG algorithm	—	✓	✓	✓
C&CG algorithm	✓	—	—	—
Coordinated planning	✓	✓	✓	—
Line construction cost	59.58	59.58	59.58	59.58
Investment cost of PSES	60.00	60.00	104.00	104.00
Salt spray-induced cost	2.99	2.99	4.31	4.31
Network loss cost	44.43	44.43	43.38	54.94
Carbon emission cost	225.46	225.46	217.08	223.16
Power procurement cost	3256.88	3256.88	3237.89	3251.29
Subsidy	0.00	0.00	-51.60	-51.60
Total cost	3649.34	3649.34	3614.64	3645.68
Solution time	5772.65	585.87	8599.13	35388.69

In the planning results, all cases yield identical DN topology. Since Case A and Case B differ only in the solution algorithm, the siting results for EV charging stations are also the same, with selected nodes located near the substation to reduce power losses. In Case C, three PSEs are sited adjacent to the substation and one at the feeder end (Node 24), indicating that the reduction in network losses due to PV and

ESS outweighs the additional losses induced by EV charging in residential areas. In Case D, where only DN planning is optimized and the PSEs are pre-assigned to the terminal nodes in each region (Node 9, 24, 41, 47) to maximize the operational benefits of PV and ESS.

Comparing the annualized results, Case C achieves a 2.36% reduction in power loss cost compared to Case A and Case B, attributed to the effect of PV and ESS in PSEs. Meanwhile, carbon emission and power procurement costs decrease by 3.72% and 0.58%, respectively, resulting in a total annualized cost reduction of 34.7×10^4 CNY. Compared to Case C, Case D exhibits a 26.65% increase in power loss cost and a total cost increase of 31.04×10^4 CNY. Although siting PSEs at feeder-end nodes maximizes the power loss reduction potential of PV and ESS, the increased power losses induced by EV charging offset the benefit, demonstrating the importance of coordinated planning between DN and PSEs. Under the same convergence tolerance, Cases A and B share identical cost outcomes. However, the solution time of Case B using the i-C&CG algorithm is only 10.15% of that of Case A with the conventional C&CG, validating the computational efficiency of the proposed i-C&CG algorithm.

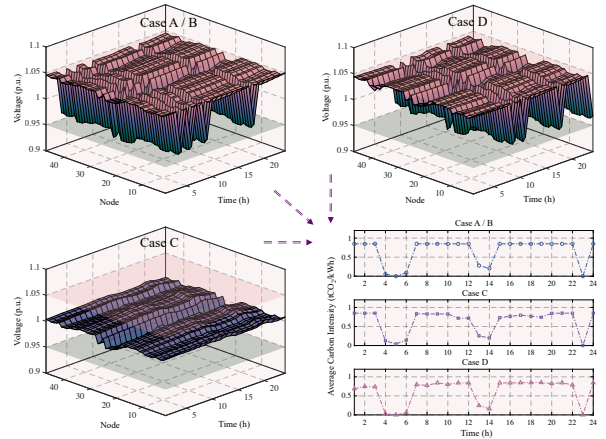


Fig. 3. Voltage and average carbon intensity fluctuations for different cases.

The variations in nodal voltage and average carbon intensity for different cases are illustrated in Fig. 3. The extreme difference of voltage for Case A/B, Case C, and Case D are 0.1000, 0.0315, and 0.1000 p.u., while the corresponding standard deviations are 0.0298, 0.0064, and 0.0300 p.u., respectively. Case C exhibits the smallest voltage extreme difference and standard deviation, indicating the most stable voltage profile and the highest voltage quality. In contrast, Case D results in larger voltage fluctuations without PSEs siting in its planning. Despite the presence of PV and ESS, the voltage variation in Case D remains more severe than that in the cases with only conventional EV charging stations, further validating the importance of coordinated planning between DN and PSEs. The average carbon intensity across all nodes and time intervals for Cases A/B, C, and D is 0.6636, 0.6367, and 0.6285 tCO₂/kWh, which indicates that the integration of PV and ESS can effectively reduce the nodal carbon intensity. Compared to siting PSEs near the substation, constructing them at feeder-end nodes in Case D will lead to lower carbon intensity of the surrounding downstream nodes, but this configuration will

increase the power losses. Therefore, planning should consider a trade-off among multiple cost components to achieve an optimal balance.

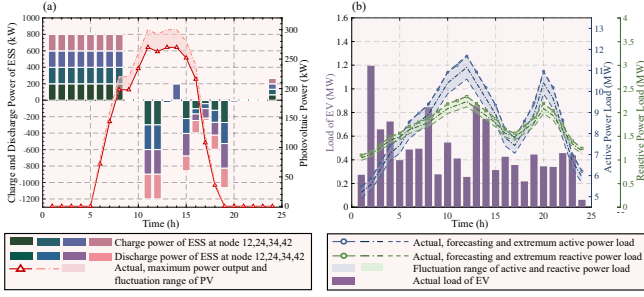


Fig. 4. (a) Operation of PV and ESS. (b) Load fluctuation errors in robust optimization.

The operational characteristics of PV and ESS, along with the load fluctuation errors under robust optimization in Case C, are illustrated in Fig. 4. It can be observed that the active and reactive power loads exhibit similar fluctuation trends throughout the day. The ESS discharges during peak load intervals and charges during low load intervals, demonstrating its effectiveness in peak shaving and valley filling within DN. The PV output eventually reaches its lower bound of 0.9 and operates at full capacity in all time intervals, indicating the proposed model is capable of attaining the optimal solution under the worst-case scenario. The EV charging load exhibits a fluctuation pattern that is broadly similar, though not identical, to that of the active and reactive loads, highlighting the effectiveness of electricity price-driven orderly charging strategies for EV users.

B. Sensitivity Analysis of Different Parameters

Fig. 5 shows the variations in different cost components with increasing load fluctuation and EV penetration defined in [6]. As both load and EV penetration increase, power losses and total costs rise accordingly. However, the DN topology remains unchanged, confirming the planning framework's robustness to accommodate future growth in EV penetration.

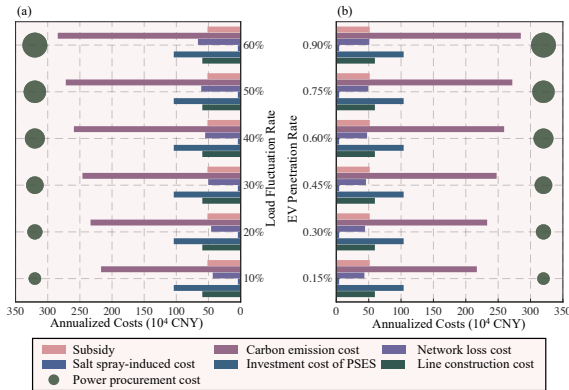


Fig. 5. Sensitivity analysis of load fluctuation and EV penetration.

The sensitivity analysis of the key parameters in both RO and DRO models is shown in Fig. 6. As RO aims to optimize under the worst-case scenario, it yields the most conservative solution, resulting in the highest total cost. In the DRO framework, larger values of the EV number fluctuation parameters α_1 and α_∞ indicate increased uncertainty in the

expected number of EVs. Similarly, higher values of the variance σ and confidence level $1 - \alpha$ used to model EV charging power in the truncated normal distribution imply increased variability. As the confidence level approaches 1, the DRO model becomes more similar to RO. Since DRO considers the worst-case distribution within an ambiguity set, the total cost escalates as the related uncertainty parameters grow. Compared to RO, DRO more accurately reflects the empirical distribution of EV charging data while preserving robustness against adverse scenarios.

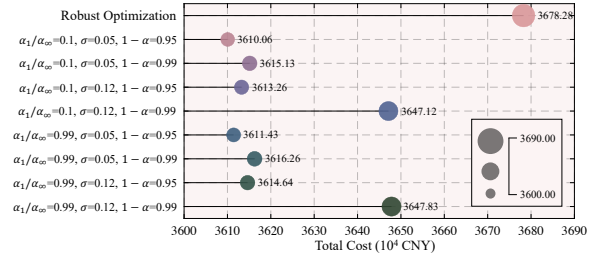


Fig. 6. Sensitivity analysis of distributionally robust parameters.

C. Analysis of Tidal Current Units in Coastal Cities

Tidal energy output varies with tidal velocity, peaking between high and low tides under the semi-diurnal tide model. Although higher tidal output generally lowers its electricity price, the levelized cost of tidal units remains above that of thermal generators due to their high life-cycle costs. As shown in Fig. 7(a), tidal power is preferred for procurement when its electricity price is relatively low. Conversely, when the tidal electricity price significantly exceeds that of thermal power, it will not be selected.

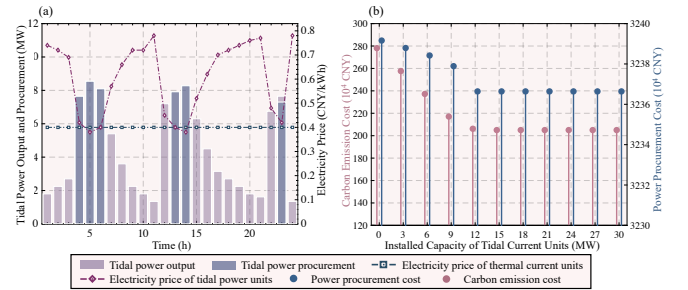


Fig. 7. (a) Power output, procurement and electricity price. (b) Sensitivity analysis of the installed capacity of tidal current units.

Fig. 7(b) presents the sensitivity analysis of installed tidal capacity. Increasing capacity up to 15 MW markedly reduces both carbon emissions and procurement costs, lowering the total system cost. Notably, the scenario with 0 MW installed capacity can be regarded as a non-coastal city. However, once the installed capacity exceeds 15 MW, due to the pricing mechanism of tidal electricity, further expansion does not result in additional tidal power procurement, as it would no longer contribute to minimizing the total cost. These results highlight that the development of low-carbon coastal cities requires substantial government support for renewable energy generation in order to reduce the levelized cost of electricity for sources such as tidal energy.

V. CONCLUSION

This paper proposes a coordinated planning framework for DN and PSES in low-carbon coastal cities, with the CEF

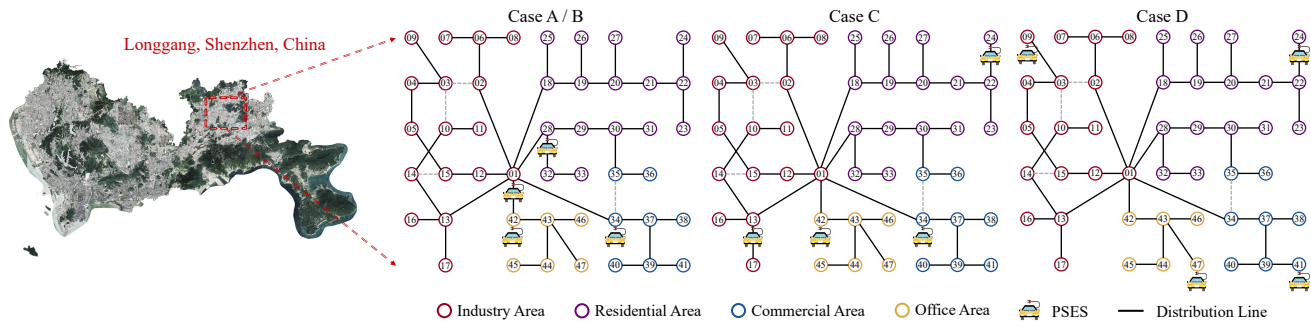


Fig. 8. Planning solutions for different cases in Longgang District, Shenzhen, China.

model used to quantify carbon emissions and tidal energy incorporated as an emerging renewable source. The framework considers various uncertainty sets, including continuous ambiguity sets for active/reactive load and PV generation, as well as discrete distributions for the number of EVs. A comprehensive norm is used to constrain the distributionally robust ambiguity sets.

To handle the non-convexity introduced by ESS-related binary variables in the mid-layer, a tailored relaxation method is proposed and rigorously validated. The i-C&CG algorithm is introduced to solve the model efficiently, ensuring finite-time convergence and notably improving computational efficiency.

Case studies demonstrate that utilizing tidal energy effectively reduces both carbon emissions and overall system cost, providing valuable insights for policy initiatives aimed at promoting marine renewable energy development in coastal regions. Furthermore, the high cost-effectiveness of PV and ESS in PSES indicates a promising trend for future EV charging station deployment. Future work may focus on integrating additional renewable sources such as offshore wind to further enhance modeling accuracy and strategic planning capabilities for coastal energy systems.

REFERENCES

- [1] W. Lee, L. Xiang, R. Schober, and V. W. Wong, "Electric vehicle charging stations with renewable power generators: A game theoretical analysis," *IEEE Transactions on Smart Grid*, vol. 6, no. 2, pp. 608–617, 2014.
- [2] M. Li, S. Cao, X. Zhu, and Y. Xu, "Techno-economic analysis of the transition towards the large-scale hybrid wind-tidal supported coastal zero-energy communities," *Applied Energy*, vol. 316, p. 119118, 2022.
- [3] A. Ahmadian, M. Sedghi, and M. Aliakbar-Golkar, "Fuzzy load modeling of plug-in electric vehicles for optimal storage and dg planning in active distribution network," *IEEE Transactions on Vehicular Technology*, vol. 66, no. 5, pp. 3622–3631, 2016.
- [4] Y. Xiang, P. Xue, Y. Wang, L. Xu, W. Ma, M. Shafie-Khah, J. Li, and J. Liu, "Distributionally robust expansion planning of electric vehicle charging system and distribution networks," *CSEE Journal of Power and Energy Systems*, 2023.
- [5] X. Shi, Y. Xu, Q. Guo, Y. Sheng, H. Sun, F. Chen, and Y. Zhang, "Novel planning approach for fast-charging station in integrated system," *CSEE Journal of Power and Energy Systems*, vol. 9, no. 5, pp. 1832–1844, 2022.
- [6] Y. Wang, X. Shen, and Y. Xu, "Joint planning of active distribution network and ev charging stations considering vehicle-to-grid functionality and reactive power support," *CSEE Journal of Power and Energy Systems*, vol. 10, no. 5, pp. 2100–2113, 2023.
- [7] Y. Wang, X. Shen, and W. Gao, "Integrated planning of urban distribution network and multi-charging infrastructures with smart transportation system," *Available at SSRN 5185181*.
- [8] C. Sun, X. Zhao, B. Qi, W. Xiao, and H. Zhang, "Economic and environmental analysis of coupled pv-energy storage-charging station considering location and scale," *Applied Energy*, vol. 328, p. 119680, 2022.
- [9] Y. Cheng, N. Zhang, Z. Lu, and C. Kang, "Planning multiple energy systems toward low-carbon society: A decentralized approach," *IEEE Transactions on Smart Grid*, vol. 10, no. 5, pp. 4859–4869, 2018.
- [10] Z. Ren, Y. Wang, H. Li, X. Liu, Y. Wen, and W. Li, "A coordinated planning method for micro-siting of tidal current turbines and collector system optimization in tidal current farms," *IEEE Transactions on Power Systems*, vol. 34, no. 1, pp. 292–302, 2018.
- [11] S. Porkar, P. Poure, A. Abbaspour-Tehrani-fard, and S. Saadate, "A novel optimal distribution system planning framework implementing distributed generation in a deregulated electricity market," *Electric Power Systems Research*, vol. 80, no. 7, pp. 828–837, 2010.
- [12] P. Zare, A. Dejamkhooy, S. S. Majidabad, and I. F. Davoudkhani, "Stochastic milp model for merging ev charging stations with active distribution system expansion planning by considering uncertainties," *Electric Power Components and Systems*, pp. 1–31, 2023.
- [13] J. Zhao, J. Qu, H. Ji, J. Xu, H. M. Hasanien, R. A. Turkey, and P. Li, "Robust operation of flexible distribution network with large-scale ev charging loads," *IEEE Transactions on Transportation Electrification*, vol. 10, no. 1, pp. 2207–2219, 2023.
- [14] H. T. Nguyen and D.-H. Choi, "Decentralized distributionally robust coordination between distribution system and charging station operators in unbalanced distribution systems," *IEEE Transactions on Smart Grid*, vol. 14, no. 3, pp. 2164–2177, 2022.
- [15] Y. Shui, J. Liu, H. Gao, G. Qiu, W. Xu, and J. Gou, "Two-stage distributed robust cooperative dispatch for integrated electricity and natural gas energy systems considering uncertainty of wind power," *Automation of Electric Power Systems*, vol. 42, no. 13, pp. 43–50, 2018.
- [16] H. Gao, X. Lyu, S. He, L. Wang, C. Wang, and J. Liu, "Integrated planning of cyber-physical active distribution system considering multi-dimensional uncertainties," *IEEE Transactions on Smart Grid*, vol. 13, no. 4, pp. 3145–3159, 2022.
- [17] B. Zeng and L. Zhao, "Solving two-stage robust optimization problems using a column-and-constraint generation method," *Operations Research Letters*, vol. 41, no. 5, pp. 457–461, 2013.
- [18] M. Y. Tsang, K. S. Shehadeh, and F. E. Curtis, "An inexact column-and-constraint generation method to solve two-stage robust optimization problems," *Operations Research Letters*, vol. 51, no. 1, pp. 92–98, 2023.
- [19] S. Li and L. Shi, "A tri-level day-ahead spatio-temporal defense strategy against coordinated cyber-physical attacks with high wind power penetration," in *2024 IEEE Power & Energy Society General Meeting (PESGM)*. IEEE, 2024, pp. 1–5.
- [20] L. Du, J. Chen, E. Hu, and F. Zeng, "A reactive molecular dynamics simulation study on corrosion behaviors of carbon steel in salt spray," *Computational Materials Science*, vol. 203, p. 111142, 2022.
- [21] Y. Wang, Y. Xu, J. Li, J. He, and X. Wang, "On the radiality constraints for distribution system restoration and reconfiguration problems," *IEEE Transactions on Power Systems*, vol. 35, no. 4, pp. 3294–3296, 2020.
- [22] C. Zhao and Y. Guan, "Data-driven stochastic unit commitment for integrating wind generation," *IEEE Transactions on Power Systems*, vol. 31, no. 4, pp. 2587–2596, 2015.
- [23] C. Yang, J. Liu, H. Liao, G. Liang, and J. Zhao, "An improved carbon emission flow method for the power grid with prosumers," *Energy Reports*, vol. 9, pp. 114–121, 2023.